Polymer 51 (2010) 2769–2778

Contents lists available at ScienceDirect

Polymer

journal homepage: www.elsevier.com/locate/polymer

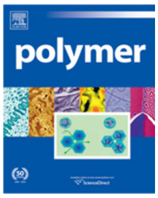

Barb formation in electrospinning: Experimental and theoretical investigations

A. Holzmeister [a], A.L. Yarin [b,c], J.H. Wendorff [a,*]

[a] Department of Chemistry and Center of Material Science, Philipps-Universität Marburg, Marburg, Germany
[b] Department of Mechanical and Industrial Engineering, University of Illinois at Chicago, 842 W Taylor St., Chicago IL 60607-7022, USA
[c] Center of Smart Interfaces, Technische Universität Darmstadt, Petersenstr. 32, 64287 Darmstadt, Germany

ARTICLE INFO

Article history:
Received 25 February 2010
Received in revised form
30 March 2010
Accepted 2 April 2010
Available online 14 April 2010

Keywords:
Barbed nanofibers
Morphology
Electrospinning

ABSTRACT

PVA nanofibers electrospun from solutions with relatively low polymer concentrations (below 8 wt%) tend to be no longer smooth, but display barbs which occur regularly spaced along the nanofiber length. Such structures are of interest for a number of technical applications, since they affect the fiber packing, pore sizes and the internal surfaces in the nanofiber nonwovens. This paper reports both, experimental and theoretical results, allowing to elucidate the mechanism responsible for barb formation. It is found that barb formation can be explained theoretically in terms of a relatively slow charge relaxation within the jet compared to the development of the secondary electrically driven instabilities which locally deform the jet surface. Both, the electric conductivity of polymer solutions and their viscoelasticity, are key parameters controlling the competition between charge relaxation and rate of growth of capillary and electrically driven, secondary, localized perturbations of the jet surface and thus barb formation. In this paper a nonlinear theoretical model is proposed that is able to mimic the main morphological trends recorded in the experiments.

1. Introduction

Electrospinning is one of the few fiber producing techniques that transform an original macroscopic feeding volume of polymer melt or polymer solution into final solidified nanofibers. The process is predominantly controlled by the electric charges and fields in contrast to the conventional extrusion techniques relying on mechanical forces [1–5]. In contrast, in melt or dry/wet solution spinning the shape and diameter of the die, as well as mechanical forces inducing specific draw ratios and drawing speeds determine dimensional and structural properties of the resulting fibers to a major extent. These technical differences in the fiber formation processes may be exploited in the case of electrospinning to come up with novel types of fiber morphologies.

It is certainly true that fibers produced via electrospinning may resemble in many aspects the ones produced by melt or solution blowing. Fibers can be produced in both cases in the micrometer range with the cross-sectional area displaying a circular shape and the fiber surface being smooth. Yet it is also true that by taking full advantage of the specific features characteristic of electrospinning, one can produce fibers with diameters down to a few nanometer, fibers which have been subjected in the course of their production to extremely strong elongational deformations yielding fibers with high longitudinal orientation of crystals and chain macromolecules directly during the spinning process [1]. These features originate from the onset of the electric charge-induced bending instabilities well documented in the literature [5–7]. Furthermore fibers may be prepared in a controlled way displaying beads along their length as induced by an axisymmetric instability again controlled by the presence of electric charges [8,9].

A further feature sometimes observed in fiber formation in electrospinning is branching. Thin jets start to emerge from the main jet with the axis of the thin secondary jet being oriented almost perpendicular to the one of the primary jet. This secondary instability accompanying the primary bending instabilities, can happen quite regularly along the jet if the electrospinning conditions are chosen appropriately as reported in the literature [10,11]. Again such branching is a direct consequence of the presence of surface charges on the jet surface, as well as of the externally applied electric field. Such branching phenomena have been modeled in terms of undulations occurring for the surface of the jet as controlled by the balance of electric and surface forces. The stability analysis predicts a quasi-regular spacing of the branches along the jet [11]. In all examples given above, the key role of the electric charges present at the jet surface and their interactions with the external electric field was fully uncovered and explained.

In fact, such basic fiber forming processes characteristic for electrospinning can be rationalized in terms of the general Earnshaw's theorem of electrostatics. According to this theorem it is

---

* Corresponding author.
E-mail address: wendorff@staff.uni-marburg.de (J.H. Wendorff).

0032-3861/$ – see front matter © 2010 Published by Elsevier Ltd.
doi:10.1016/j.polymer.2010.04.005

impossible to create any stable structures (including stable liquid jets), in which all elements interact only by Coulomb forces [5,12–14]. Charges located within the fluid jet, in the case considered here, move the polymer elements to which they are attached along complex pathways in such a way that the electric field energy is minimized. Droplet deformation, jet initiation and, in particular, the bending instability which control to a major extent fiber sizes and properties are controlled apparently predominantly by this principle [5,14–16]. Taking Earnshaw's theorem into account, it seems reasonable to assume that a further still unobserved, undetected variety of fiber morphologies might be accessible via electrospinning if the processing parameters are chosen appropriately. One observation is that fiber formation, for instance in the case of polyamide (PA) 6 with diameters in the 100 nm range and above spun from formic acid, is accompanied by the formation of an ultrafine web composed of fibers with diameters of a few nm spanning the distance between two or more fibers of regular diameter size [17,18]. Such structures may originate from branching yet no details on the underlying formation processes are apparent to us.

Nanofibers produced from water and composed of polyvinylalcohol (PVA) occasionally exhibit spikes along the fibers (Fig. 1). Fibers with a regular arrangement of well defined spikes along the fiber length might be of interest for certain applications including inhalation therapy, fiber reinforcement, tissue engineering, etc. One argument is that the spikes can be used to control the average distance between fibers and thus pore diameters and subsequently permeability of nanofiber mats. Another argument might be that spikes allow control of the specific surface area, which is of interest for applications relying on adsorption/desorption processes [19] in catalysis (for carriers of homogeneous or heterogeneous catalysts), for modification of solid surfaces (for wettability control), control of heat dissipation [20] and many more.

It is for this reason that we have looked into spike formation in more detail in a previous publication [21]. In fact, we were able to point out conditions for which such spikes (which we called barbs and barbed nanofibers) regularly spaced along the fiber length can be introduced in a reproducible way. We also pointed out in which way the shape of the barbs varies as electrospinning parameters are modified. The origin of the barb formation, the possible relation of barb formation to branching phenomena were not considered in Ref. [21] and no attempt was made to rationalize experimental findings in terms of a theoretical model. Yet, in view of trying to elucidate the access to a novel type of nanofiber morphology and nanofiber nonwoven architecture, as well as in view of possible applications of such barbed nanofibers and related structures, it is worth to look deeper into the basic mechanisms controlling barb formation. This is the aim of the present work, which involves a combination of more detailed experimental investigations and theoretical modeling.

2. Experimental

2.1. Polymer materials

Polyvinylalcohol "Mowiol 56-98" with molecular weight $M_w = 195$ kDa and a degree of hydrolysis of 98% and "Mowiol 28-99" with $M_w = 145$ kDa and a degree of hydrolysis of 98.4% were purchased from Kuraray Europe GmbH (Germany). In the following, they are represented as PVA 56-98 and PVA 28-99, respectively. Before use, both polymers had to be purified via dialyses. For this reason, aqueous solutions of approximately 9–10 wt% were filled into porous tubes (Spectrum Laboratories Inc., Spectra/Por, pore size: 3000 kDa) and dialyzed in double distilled water (conductivity $\sigma \leq 5$ μS/cm) for 34 h. The medium was exchanged at least three times during this period. The purified PVA was then precipitated in freshly distilled acetone and subsequently dried under vacuum at room temperature (21 °C). Using the purified PVA sample, solutions of different concentrations with relatively constant conductivities ranging between 10 and 25 μS/cm (Fig. 2) were prepared as detailed in the following section.

2.2. Spinning solutions

Stock solutions of the purified PVA in double distilled water were prepared at 90 °C with concentrations of 4 wt%, 6 wt%, 8 wt% and 10 wt%. Other concentrations were derived from these stock solutions via diluting with double distilled water.

In order to get series of different conductivities, we added small amounts of sodium chloride (NaCl) to the PVA solutions (some results are shown in Fig. 3). Yet, the best results were achieved when we added a highly conductive stock solution of NaCl and PVA ($\sigma = 3.2$ mS/cm) dropwise to a pure, low-conducting ($\sigma = 16$ μS/cm) solution. With both solutions having the same concentrations of

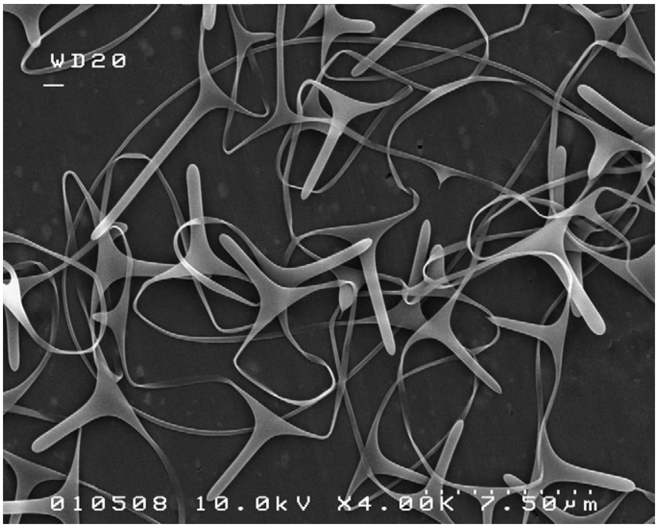

Fig. 1. PVA barbed nanowires spun from 4.5 wt% aqueous PVA 56-98 solution.

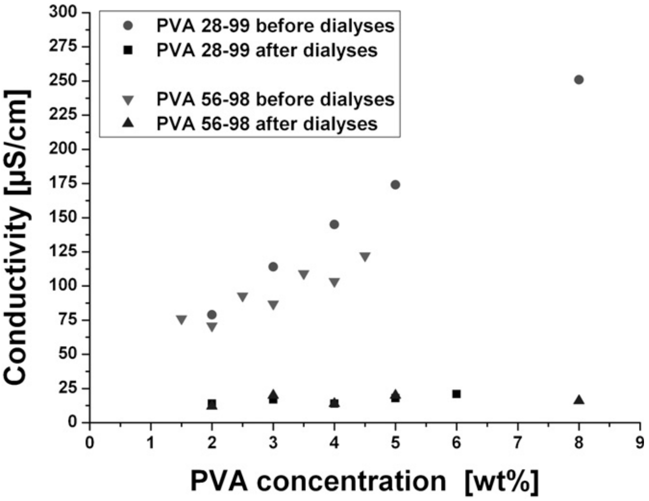

Fig. 2. Conductivity of PVA solutions before and after purification via dialyses.

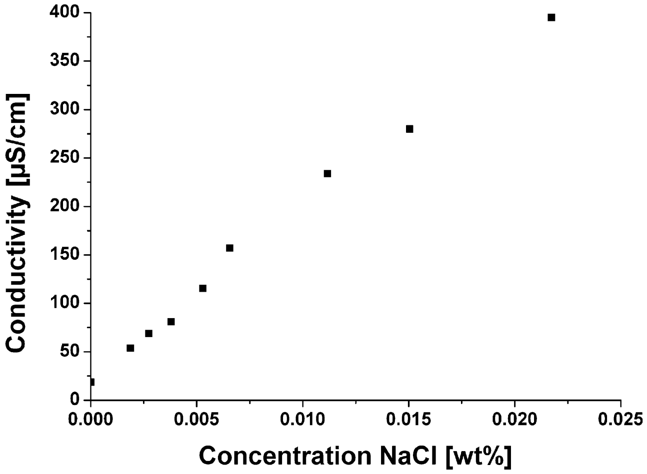

Fig. 3. Conductivity of PVA 56-98 solution (3 wt%) with increasing amount of NaCl.

PVA, the electric conductivity could be increased in small steps of about 15–20 µS/cm per drop without changing the polymer concentration.

2.3. Determination of the electric conductivity

The conductivity of the PVA/NaCl-solutions was determined with a conducting meter (inoLab Cond Level 3) using a single rod measuring cell (TetraCon 325, WTW GmbH) at 25 °C.

2.4. Determination of shear viscosity

A rotation viscometer PK 100 (Haake Messtechnik GmbH&Co) was used in the cone/plate mode to determine the shear viscosity of the PVA solutions at 3000 s^{-1} at 21 °C. One drop (~0.5 mL) of solution was placed for this purpose on the substrate and the cone (Haake PK 1, angle: 1°) was positioned at a distance of 0.6 mm. *Rheowin* software was used to process the data.

2.5. Electrospinning setup and conditions

The experimental apparatus used in the work discussed below was a conventional setup for electrospinning of nanofibers. Polymer solutions were pumped through a thin capillary acting as a die with an inner diameter of 600 µm. The die simultaneously served as an electrode to which a high electric field was applied. Whilst the distance to the counter-electrode was kept constant at 15 cm (if not explicitly mentioned otherwise), feeding rates and electric field strengths were chosen to be in the range of 0.3–0.6 mL/h and 100–130 kV/m, respectively, depending on the polymer solutions. These values allowed a constant electrospinning process resulting in continuous fiber formation. The electric current during electrospinning was of the order of 100 nA. All electrospinning experiments where performed at room temperature (19–21 °C) and low relative humidity <30%.

The experiments concerning different conductivities of 3.5 wt% PVA 28-99 solutions at a spinning distance of 15 cm were performed under the conditions listed in Table 1, where U is the applied voltage and E the electric field strength.

2.6. Scanning electron microscopy

The resulting nanofibers were analyzed by SEM (scanning electron microscopy) with a Hitachi 4001 SEM (acceleration voltage of 8 kV), a Jeol JSM 5610OLV (acceleration voltage of 2 kV) and a Cambride Scanning Company CamScan4DV (acceleration voltage of 15 kV) and subsequently evaluated graphically with *ImageJ*. The three types of SEMs we used differ in resolution (see acceleration voltage). For survey images we used the SEM with lower resolution, to obtain details of fiber structure and diameters we used higher resolution SEMs.

3. Experimental results

First of all, it should be pointed out that we did not observe differences concerning the barb lengths when using either PVA 28-99 and PVA 56-98 in the spinning solutions. Thus in the following, the tendencies discussed in relation to the shape of the barbs, are basically the same for both types of polymers: the differences in molecular weight obviously have no significant effect. However, we also want to add that, as far as lower molecular weights of PVA are concerned, we found that the range of molecular weights for which barb formation occurs is limited. For example, for PVA with a molecular weight even as high as 61 kDa, we only observed bead formation. So in view of this, the variation in molecular weight considered here is significant and the finding we want to point out is, that in this range the molecular weight does not play a role.

In electrospinning the shape and dimension of the fibers are known to be strongly correlated to the spinning conditions. In our previous paper on barbed nanowires we considered the polymer concentration in the spinning solution as one of the main factors of influence [21]. Yet, only the occurrence of barbed nanofibers and the magnitude of the barb diameter have been examined in detail previously. With the following experiments we extend these studies, and report on the influence of key parameters of electrospinning such as electrode distance/electric field, feeding rate, polymer concentration/shear viscosity and conductivity on barb formation. Barb length rather then its diameter was chosen as most significant characteristic in these studies. It is defined as shown in Fig. 4.

Since the surface tension of PVA solutions for the concentrations used in the present work is approximately constant (in the range of 60–70 N/m), we did not study the influence of surface tension on barb formation. When varying the collection distance, the electric field strength and feeding rate in the ranges given above, no significant variations in the overall occurrence and the length of the barbs were apparent. We, therefore, assume that either there is no influence of these parameters or more likely, the range of parameters for which stable electrospinning was achieved is too narrow. For example, a sustainable jet could only be achieved for electrode distances between 15 and 20 cm. Given the fact that the true spinning distance depends on the total distance between the nozzle and the spot where the nanofiber is finally deposited onto the disk-like counter-electrode (which had a diameter of ~12 cm) and thus varies anyway to some extent, a difference in the adjustable inter-electrode distance of 5 cm is insignificant. Fig. 5a shows the resulting barb length at the minimal and maximal

Table 1
The electrospinning conditions for different PVA 28-99 ($c = 3.5$ wt%) solutions.

σ [µS/cm]	16	30	50	84	108	157	195	253	305	378	494	641	1734
U [kV]	17.1	17.1	17.1	15.5	16.0	16.0	19.0	19.5	17.5	21.5	21.5	22.5	27.5
E [kV/m]	114.0	114.0	114.0	103.3	106.7	106.7	126.7	130.0	116.7	143.3	143.3	150.0	183.3

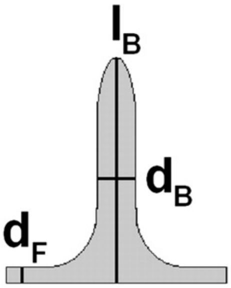

Fig. 4. Geometric definitions: l_B-barb length, d_B-barb diameter, d_F-fiber diameter.

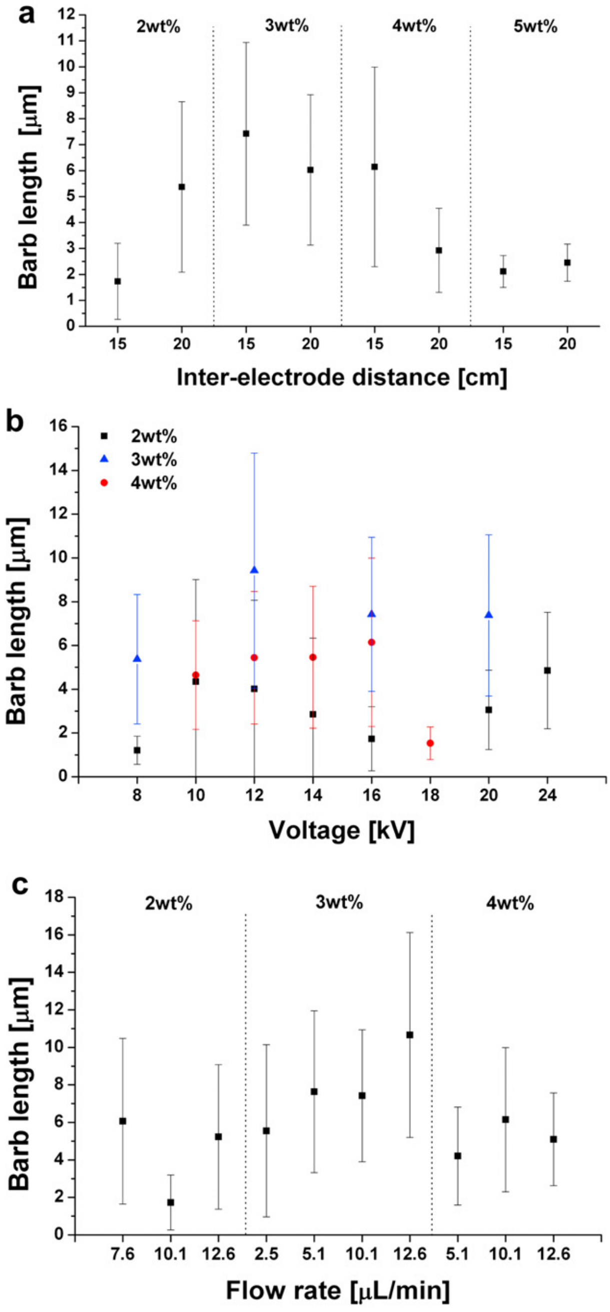

Fig. 5. Barb length vs. the inter-electrode distance (a), voltage (b) and flow rate (c) for PVA 56-98 solutions.

possible distance confirming that this change had no remarkable influence, especially when standard deviations are considered. When the spinning distance was kept constant at 15 cm and the applied voltage was varied between 0.5 and 1.6 V/cm, no effect could be seen regarding the barb length. Instead the data seemed to be randomly scattered as is seen in Fig. 5b. However, the data also give a first hint that concentration is more important for the barb formation process than the parameters considered so far.

Similar results were found when different feeding rates were applied (Fig. 5c). Again, no clear trend or change can be defined.

So it seems that neither inter-electrode distance, nor voltage and flow rate control barb formation to a major extent.

This does not hold, however, for the shear viscosity of the spinning solutions. Fig. 6 shows the dependence of the solution shear viscosity on polymer concentration at a fixed shear rate of 3000 s^{-1}. The intermediate domain shows the concentration range in which barb formation was observed. It is obvious that barbs can only be formed if the concentration of the solution is kept below 6 wt% which corresponds to a shear viscosity below 150–200 mPa s at this shear rate. If the viscosity is decreased further, the fiber and barb formation disappear at once and electrospraying rather than electrospinning takes place. On the other hand, at higher shear viscosity values, the solutions are so concentrated that viscoelastic effects become so pronounced that they suppress localized elongational flows controlling barb formation. For convenience and an easier comparison, we will stick to polymer concentration when talking about barb and shear viscosity relations, since we did the same in our previous paper [21]. We have, however, to point out a problem encountered in most papers on electrospinning as far as the rheological properties are concerned. It is well known, that electrospinning involves extremely high deformation rates and it involves elongational flow processes. So, for the illustration of some rheological peculiarities, shear viscosities at higher shear rates are usually chosen in order to compare different spinning solutions, as is done in the present work. In the relatively rare works where comprehensive rheological information is provided for electrospinning solutions, in addition to simple shear also the uniaxial elongational rheometry is used, which allows for measuring viscoelastic relaxation time [13]. However, the uniaxial elongational rheometry was not attempted in the present work.

Barb and fiber diameter were plotted versus concentration in Fig. 7 and it is apparent that our earlier results could be reproduced. The diameter of barbs is always larger than the corresponding fiber diameter and increases to a higher extent with increasing polymer

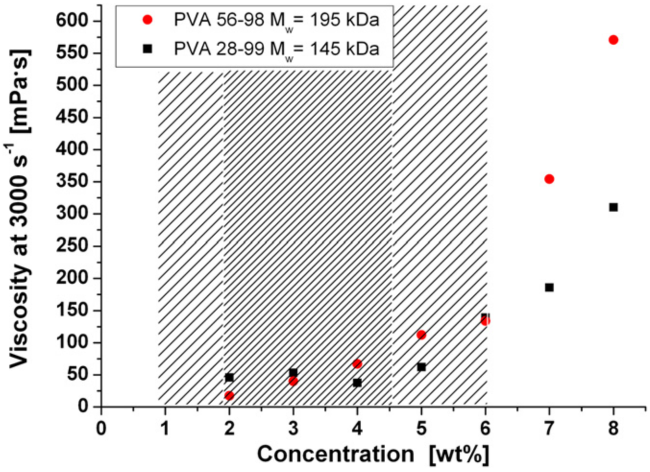

Fig. 6. Solution shear viscosity (at 3000 s^{-1}) vs. polymer concentration.

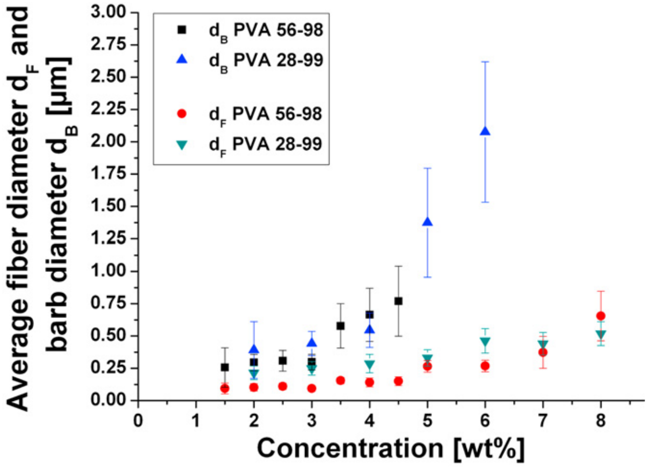

Fig. 7. Barb and fiber diameter vs. polymer concentration.

concentration than the latter until the concentration is too high to allow barb formation (Fig. 7).

Fig. 8 shows that as the polymer concentration decreases from 6 wt%, barb lengths initially increase, since the decreased concentration results in lower viscoelasticity, which facilitates stretching. However, after the maximum of barb length has been achieved at 3 wt% concentration, the barb length begins to decrease and in the densely shaded domain below 2.4 wt% in Fig. 8, more and more spindle-like fibers occur together with barbs. The latter means that the viscoelastic stresses are reduced to that extent that capillary instability catches up with the electrically driven instabilities. At very low polymer concentration jet formation practically disappears and electrospraying sets in. Fig. 9 illustrates these results via the corresponding SEM images and sketches that depict the morphologies observed at different polymer concentrations. In Fig. 9a and b results for two higher (than in Fig. 8) concentration values (8 wt% and 7 wt%) are included. They show that the viscoelastic stresses are so high at these concentrations that they prevent practically all secondary electrical and capillary instabilities, except the bending instability responsible for nanofiber formation. As a result, these nanofibers are either completely smooth or slightly squeezed. Fig. 9 illustrates that in the 6–4 wt% polymer concentration range, only barbed fibers could be found, whilst at 3 wt% the first spindle-like structures where formed in addition to barbs. Below 3 wt% some barbs grew very long with the hook-like shapes depicted in Fig. 9g. However, due to an increasing fraction of the undeveloped and, thus, shorter barbs, the overall average barb length is prone to decrease. Fig. 9g also shows that besides some barbs most of the fibers exhibited spindle-like shapes, which were not considered for the data in Fig. 8.

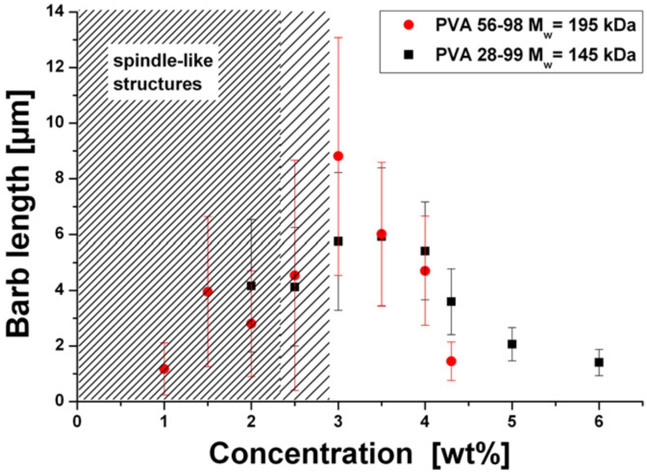

Fig. 8. Barb length vs. polymer concentration for both polymers used in the present work. The densely shaded domain on the left indicates the regime where more and more spindle-like fibers occurred.

Studies with different solution conductivities were performed for conditions listed in Table 1. The results show that one has to apply higher voltage/electric strength to solutions with higher conductivity in order to maintain a continuous electrospinning process and to induce barb formation. These experiments revealed that in addition to shear viscosity (in fact, viscoelasticity) and concentration, the electric conductivity seems to be another key parameter. As shown in Figs. 10 and 11, with increasing conductivity the barbs not only decreased dramatically in length but also more and more beads instead of barbs are formed. The data also reveal that the slightest change in conductivity has a major effect on the barb shape, especially at very low values.

Combined data characterizing the effect of conductivity and shear viscosity on the barb length are presented in Fig. 12. The occurrence of barbs is limited to a narrow domain defined by these parameters. In general, low concentrations/shear viscosities and very low conductivities favor the appearance of barbs (Fig. 13).

We also determined the distance between the barbs for a 4 wt% PVA 56-98 solution. It turned out that the barbs are arranged regularly along the nanofibers with an average distance of 17.8 ± 3.4 μm between them.

4. Theoretical

4.1. Physical estimates

Electrospun jets appear due to the action of stretching in a capacitor-like electric field [5,13,22]. The primary bending instability sets in if the electric charge on the jet is sufficiently large, while the electric conductivity low [5,13]. The bending instability leads to dramatic stretching and thinning of polymer jets towards nano-scale in cross-section. Electrospun jets are also subjected to shape perturbations resembling undulations [11], which can be the origin of various secondary instabilities leading to nonlinear morphologies developing on the jets. In the absence of the electric field only the axisymmetric undulations can grow on low-speed (relative to air) jets. In that case the undulations are enhanced by surface tension resulting in the Rayleigh capillary instability, which manifests itself in formation of the axisymmetric almost spherical beads on low viscosity liquid jets or spindle-like structures on highly viscous jets [23]. For sufficiently dilute polymer solutions with shear viscosity up to 10 times that of water (PVA 28-99 and PVA 56-98 in the concentration range 2–6 wt% where liquid spinnability/viscoelasticity is already sufficient for electrospinning), the characteristic hydrodynamic time of bead formation is of the order of $\tau_H = (\rho a^3/\gamma)^{1/2}$ where ρ and γ denote density and surface tension and a is the characteristic jet cross-sectional radius. On the other hand, when the electric field is applied, as in electrospinning, jets are charged. The charges (ions), can move inside the jet, which corresponds to conductive electric current, which tends to relax charge concentration and thus diminish the effects of the surrounding capacitor electric field on the growing undulations. However, the characteristic charge relaxation time $\tau_C = \epsilon\epsilon_0/\sigma$, with ε and σ being the relative permittivity and electric conductivity (SI units are used; ε_0 is permittivity of vacuum), may be much larger than τ_H. Then, charge relaxation is negligible during the

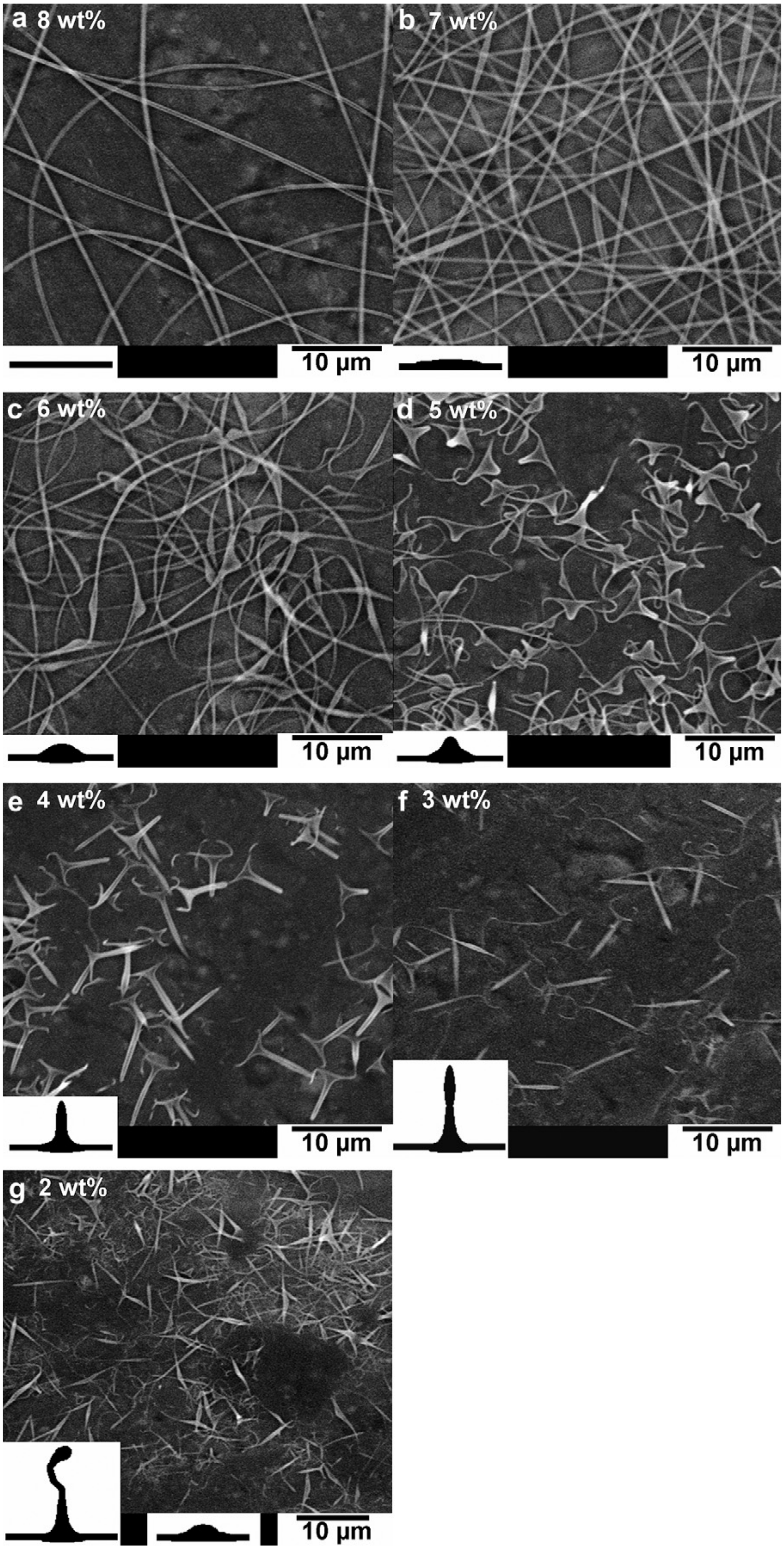

Fig. 9. SEM images of fiber morphologies at different PVA 28-99 concentrations. The sketches in the lower left corners depict the corresponding SEM observations. a) 8 wt%: smooth fibers, b) 7 wt%: slightly squeezed fibers, c–e) 6–4 wt%: barbed fibers, f) threshold value of 3 wt%: the longest average barb length and first appearance of spindle-like fibers together with long barbs, g) 2 wt%: high fraction of spindle-like fibers and shorter barbs. Some of the residual barbs where quite long ($l_B > 10$ µm) and had a hook-like shape.

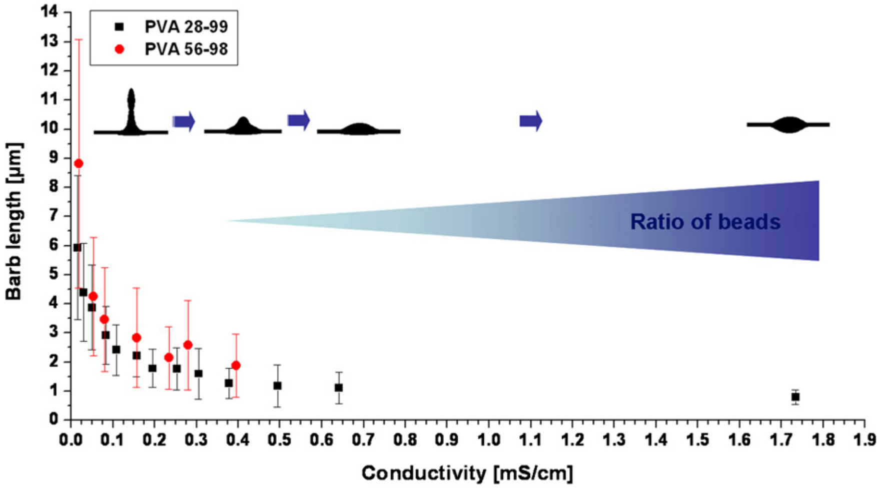

Fig. 10. Barb length vs. electric conductivity for both polymers used in the present study. Concentrations: c(PVA 56-98) = 3.0 wt%, c(PVA 28-99) = 3.5 wt%.

relevant hydrodynamic time, the liquid behaves as a dielectric, and the growing undulations of the jet surface are subjected to strong electric forces resulting from charge–charge repulsion and the action of the capacitor electric field, whereas the electric charges are practically frozen in the jet surface. As a result, strong deformations of the jet undulations by the electric forces are expected, which may take the shape of barbs in “barbed electrospun polymer nanowires” observed in the experiments in [21]. The nonlinear theory in the following subsection reveals this scenario indeed.

The above condition of barb formation, $\tau_C > \tau_H$,

$$\left(\frac{\rho a^3}{\gamma}\right)^{1/2} < \frac{\epsilon\epsilon_0}{\sigma} \tag{1}$$

means that relatively low-conducting, almost dielectric solution jets are prone to barb formation. Therefore, there exists a critical electric conductivity above which barb formation is impossible. This is indeed true according to the experimental data in Figs. 10 and 11.

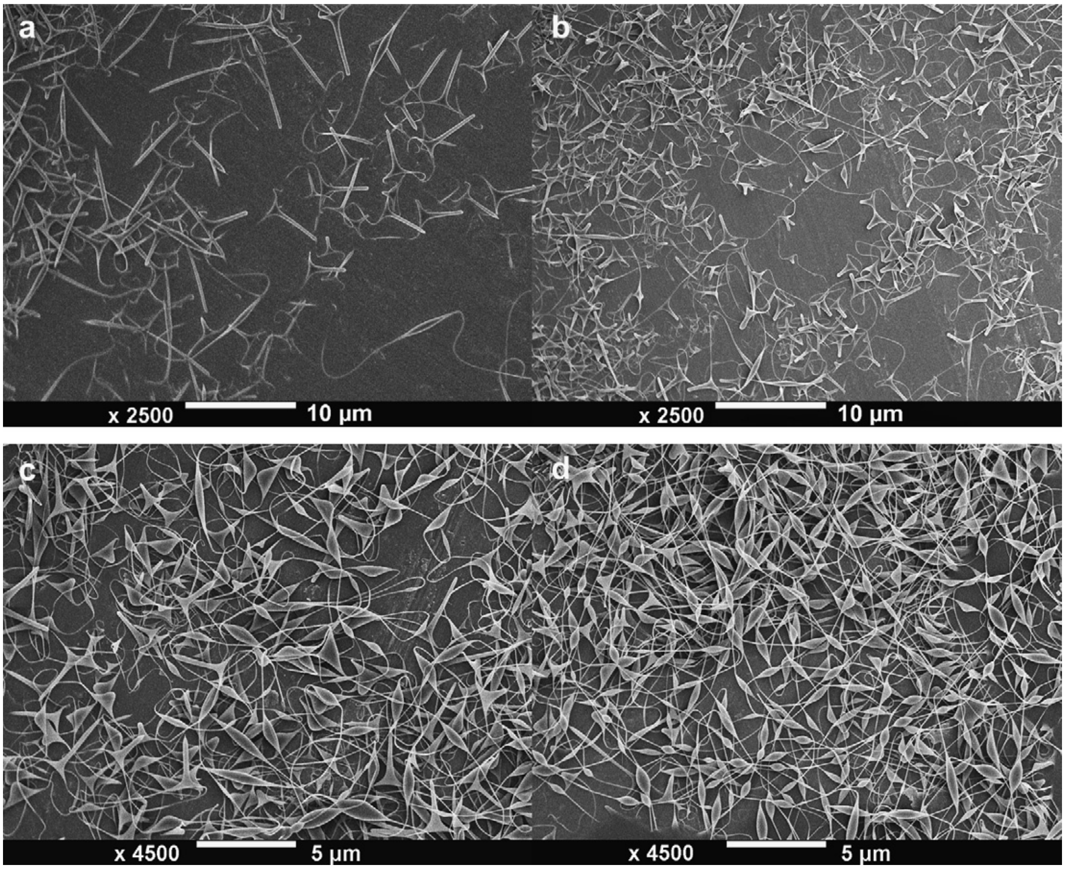

Fig. 11. SEM images of barbs of a 3.5 wt% solution of PVA 28-99 at different conductivities. (a) 16 µS/cm (b) 305 µS/cm (c) 641 µS/cm (d) 1734 µS/cm.

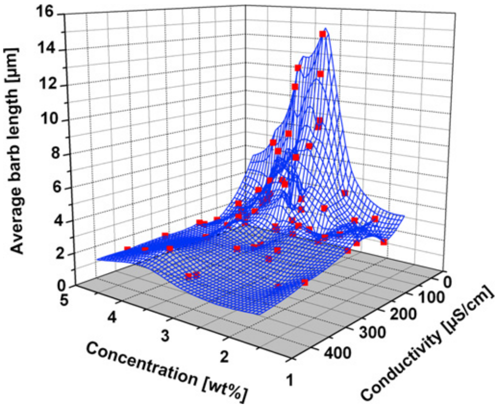

Fig. 12. Combined effect of concentration and conductivity on the barb length (blue lines are there to guide the eye only) (For interpretation of the references to colour in this figure legend, the reader is referred to the web version of this article).

Equation (1) can also be recast as a condition imposed on the jet cross-sectional radius, which means that barbs might be expected for thinner jets with $a < a_{\text{crit}}$ where a_{crit} is given by

$$a_{\text{crit}} = \left[\frac{\gamma}{\rho}\left(\frac{\epsilon\epsilon_0}{\sigma}\right)^2\right]^{1/3} \tag{2}$$

When polymer concentration in the electrospun solutions is increased, viscous effects become more pronounced and the characteristic hydrodynamic time is given by $\tau_H = \mu a/\gamma$ where μ is viscosity, rather than by $\tau_H = (\rho a^3/\gamma)^{1/2}$ [23]. Since the characteristic hydrodynamic time in viscosity-dominated cases is increasing with μ, which in turn, increases with polymer concentration in solution, it is inevitable that at a certain critical polymer concentration the time τ_H will become larger than τ_C and the electric conductivity will be able to reduce the electric forces acting on the growing undulations. Then, there exists a critical polymer concentration above which barb formation is impossible, which is indeed true according to the experimental data in Fig. 6. The solution viscosity also increases with polymer molecular weight. Therefore, a polymer molecular weight should exist beyond which barb formation is impossible.

Summarizing, we expect that secondary electrical driven instabilities [11] trigger barb or branch formation on jets with relatively low electric conductivity and not too high polymer concentration and molecular weight. Indeed, under these conditions charge relaxation via the electric current is slow compared to hydrodynamic developments, which leads to significant electrostatic repulsions of the embedded charges, as well as to strong Coulomb forces imposed via charge interaction with the capacitor electric field, i.e. to the factors responsible for barb formation.

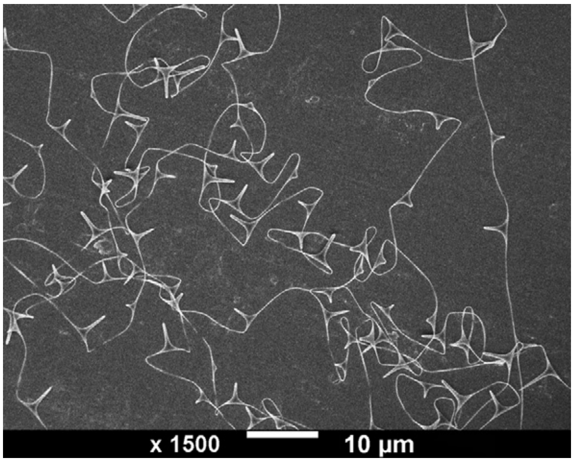

Fig. 13. Regular occurrence of barbs along fibers spun from 4 wt% PVA 56-98 (σ = 23 µS/cm).

4.2. Nonlinear model

Consider a simple two-dimensional model which elucidates the mechanism of formation of “barbed electrospun polymer nanowires” observed in the experiments in [21] and in the present work. Polymer solutions used in electrospinning are leaky dielectrics with such low electric conductivity that charge conduction in the electrospun jet can be completely neglected [5,7,13]. We adopt this approximation here, and consider a simplified two-dimensional model of a jet with a perturbed swollen cross-section and the electric charges “frozen” into the jet surface (Fig. 14). The jet is subjected to longitudinal (capacitor) electric field of strength E. The Cartesian coordinate frame xy is also “frozen” into the jet, i.e. we observe the jet moving together with it. The question to be addressed is: what will be the evolution of the shape of such jet in time? According to Earnshaw's theorem [5,24], static configuration of charges is impossible without any non-electric forces, and the jet should evolve as the charges move apart. Moving charges entrain material elements in which they are “frozen”, which can result in viscoelastic forces opposing charge motion. In the first approximation these forces will be neglected here under the assumption that the dominant role is played by the electric Coulomb forces. Then, the second law of Newton for the j-th charge takes the form

$$m\frac{d^2\boldsymbol{r}_j}{dt^2} = \sum_{i;i\neq j}\frac{1}{4\pi\epsilon\epsilon_0}\frac{q_i^2}{r_{ij}^2}\boldsymbol{e}_{ij} + q_jE\boldsymbol{i} \tag{3}$$

where m is the mass attributed to any charged material element with charge q_j, r_{ij} is the distance between the i-th and j-th charged elements (both free surfaces are accounted for; Fig. 14), $\boldsymbol{e}_{ij}$ is the unit vector of the direction from the i-th to j-th charged elements, and $\boldsymbol{i}$ is the unit vector of the x-axis (the direction of the electric field lines of the capacitor field), ϵ_0 is permittivity of vacuum and ϵ is the relative permittivity. The terms on the right hand side in Eq. (3) are written using SI units; same units are used everywhere below.

Charges should concentrate initially at the locations of the highest curvature [14], which can be mimicked by choosing $q_j = q|y_j/L|$ where y_j denotes the y-coordinates of charges at the jet

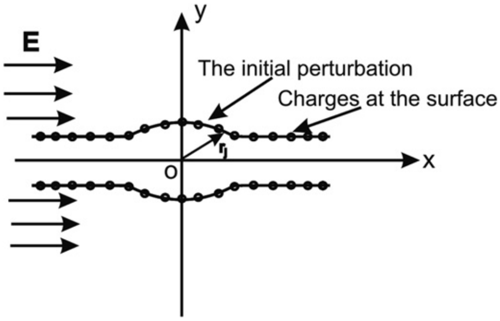

Fig. 14. Sketch of the initial configuration of the free surfaces, the capacitor electric field lines and charges “frozen” at the surfaces.

surface (cf. Fig. 14), q is the charge scale and L is the length scale. Then, Eq. (3) is projected onto the x and y-axis and takes the following dimensionless form

$$\frac{\mathrm{d}x_j}{\mathrm{d}t} = u_j \tag{4}$$

$$\frac{\mathrm{d}y_j}{\mathrm{d}t} = v_j \tag{5}$$

$$\frac{\mathrm{d}u_j}{\mathrm{d}t} = \frac{1}{4\pi\epsilon\epsilon_0}\frac{q^2T^2}{mL^3}\sum_{i;i\neq j}\frac{y_i^2(x_i-x_j)}{\left[(x_i-x_j)^2+\left(y_i-y_j\right)^2\right]^{3/2}}+\frac{qT^2E}{mL}\left|y_j\right| \tag{6}$$

$$\frac{\mathrm{d}v_j}{\mathrm{d}t} = \frac{1}{4\pi\epsilon\epsilon_0}\frac{q^2T^2}{mL^3}\sum_{i;i\neq j}\frac{y_j^2\left(y_i-y_j\right)}{\left[(x_i-x_j)^2+\left(y_i-y_j\right)^2\right]^{3/2}} \tag{7}$$

where x_j denotes the x-coordinates of the charges at the jet surface, and u_j and v_j – the x and y velocity components; the coordinates are rendered dimensionless by a length scale L, the velocity components by L/T, with T being a time scale.

Equations (4)–(7) are integrated numerically beginning from the following initial conditions at $t = 0$ for the upper free surface:

$$x = x_j,\ \ y/L = y_j/L = 1+\exp\left[-\left(x_j/L\right)^2\right],\ \ u_j = v_j = 0 \tag{8}$$

and for the lower free surface:

$$x = x_j,\ \ y/L = y_j/L = -1-\exp\left[-\left(x_j/L\right)^2\right],\ \ u_j = v_j = 0 \tag{9}$$

4.3. Modeling results and discussion

In the calculations the initial jet section is considered in the range $-10 \le x/L \le 10$. The physical parameters are chosen in the way to have $q^2T^2/(4\pi\epsilon_0\epsilon mL^3) = 0.1$ and $qT^2E/(mL)$ equal either 0 (no outside capacitor electric field is applied) or 0.5, 1 and 5 (an increasing electric field).

The system of equations (4)–(7) with the initial conditions (8) and (9) was integrated numerically using the Kutta–Merson method with the adjustable time step. The results are shown in Fig. 15a–d.

The result without any capacitor electric field along the jet axis reveals how mutual repulsion of the electric charges at the jet surfaces results in rapid growth of the initial bump, which stays

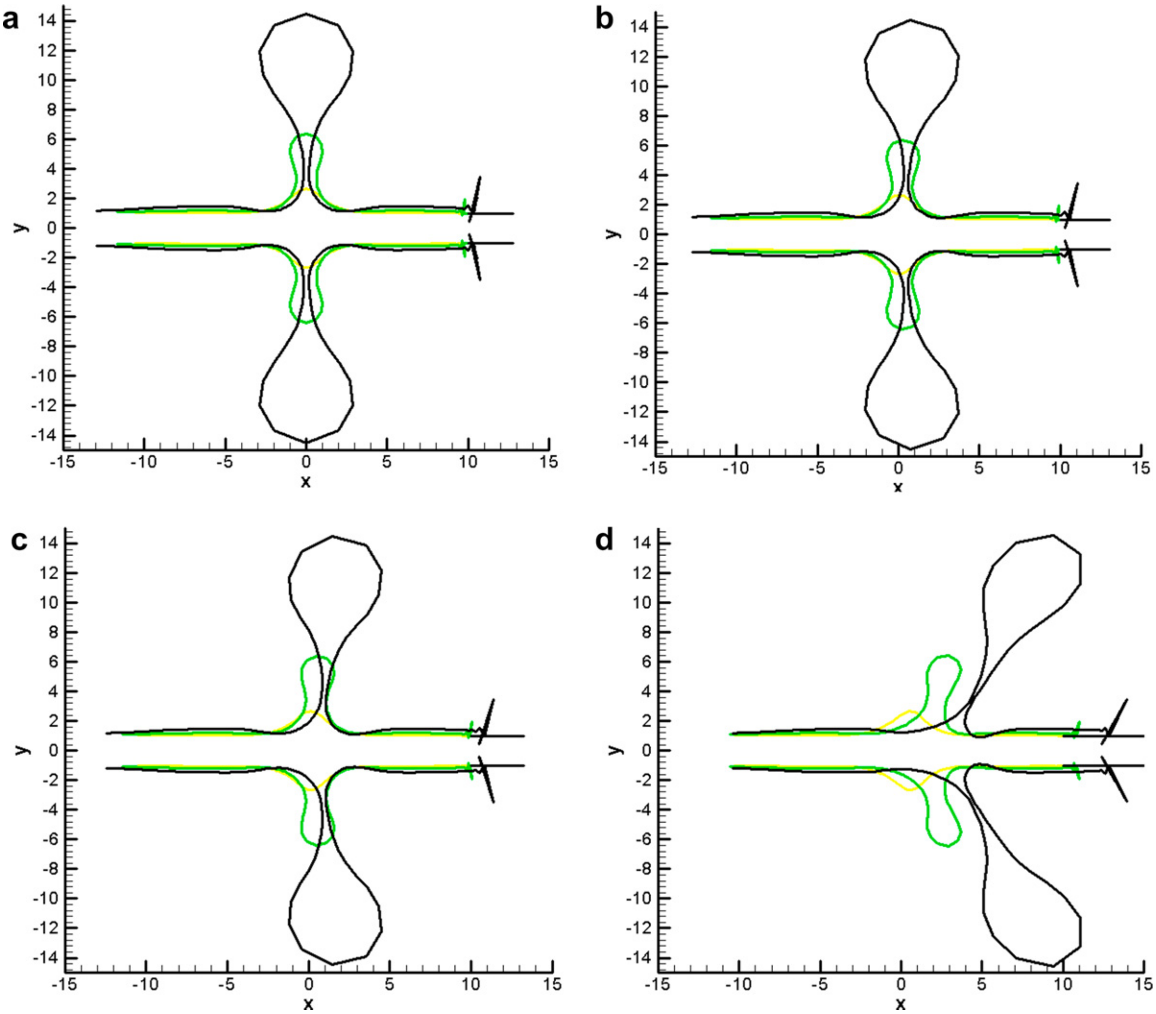

Fig. 15. Predicted evolution of the jet shape. The values of the dimensionless group $qT^2E/(\mathrm{mL})$ are: (a) 0-no capacitor field, (b) 0.5, (c) 1, and (d) 5. Correspondingly, the capacitor electric field strength increases from (a) to (d). In each frame three snapshots corresponding to $t = 0.33$, 0.66 and 0.99 are shown as yellow, green and black lines, respectively (For interpretation of the references to colour in this figure legend, the reader is referred to the web version of this article).

symmetric relative to its tip. This behavior illustrates the manifestation of Earnshaw's theorem mentioned above. On the other hand, as the longitudinal electric field increases, the jet configurations inevitably become skewed, the effect which is enhanced by increasing the field strength and is clearly visible in Fig. 15b–d. It is emphasized that both symmetric and skewed jet morphologies were observed in the previous experiments [21] and in the present work. Especially, the configurations similar to that in Fig. 15d were coined "barbed nanowires" in [21]. Note, that the spikes on the right edge of the jets depicted in Fig. 15a–d are obviously artifacts, which originate from the end effect appearing for the jets with a cut-off, i.e. the jets which do not extend to $x = \pm\infty$ and have blunt ends.

4.4. Interpretation of experiments on the basis of the theory

The experimental findings can be better understood based on the characteristic charge relaxation and hydrodynamic times. If at the jet origin the charge relaxation time is much less than the characteristic hydrodynamic time, $\tau_C << \tau_H$, their ratio varies along the jet, since τ_H decreases as the jet thins. Still, if until the solidification point the inequality $\tau_C << \tau_H$ holds, the electric conductivity is the dominant phenomenon all over the jet, and the conditions are never prone for development of secondary electrically driven instabilities, which could trigger barbs or branches. Also, the hydrodynamic capillary instability is so slow that it practically does not evolve until the jet solidification. As a result, the jet stays smooth or almost smooth. If, however, the charge relaxation time is sufficiently short to discharge jet elements, while the capillary instability accelerates due to the jet thinning and the previous strong inequality is replaced by a weaker one, $\tau_C < \tau_H$, capillary perturbation grow and beaded jets emerge (cf. Figs. 10 and 11 for the higher conductivity range). If jet thinning leads to an overtake of the decreasing τ_H by the constant τ_C, i.e. the initial inequality $\tau_C << \tau_H$, is replaced by $\tau_C \geq \tau_H$ down the jet, conductive current is diminished and strong charge–charge repulsion results in barbs (Figs. 10 and 11). If jet thinning leads to the conditions where charge relaxation becomes relatively weak, $\tau_C > \tau_H$, strong electrostatic repulsion results in longer branches on the jet (Fig. 10). Obviously, the possibility of realization of any of these cases is also affected by the value of the charge relaxation time, i.e. by the electric conductivity of polymer solution σ, and a lower σ always leads to a higher τ_C, which facilitates barb and branch formation. These cases are summarized in Table 2.

Given our experimental data (see Fig. 11), we defined $\sigma_{bead} = 2000$ μS/m and $\sigma_{barb} = 20$ μS/m as specific conductivities of 3.5 wt% solutions that resulted in beaded and barbed fibers, respectively. In addition, assume relative permittivity of these aqueous solutions being the same as for water, $\epsilon = 80$. That allowed us to determine the charge relaxation times corresponding to these solutions. Therefore, $\tau_{C,barb} = \epsilon\epsilon_0/\sigma_{barb} = 3.5 \times 10^{-4}$ ms and $\tau_{C,bead} = \epsilon\epsilon_0/\sigma_{bead} = 3.5 \times 10^{-6}$ ms. Also, assuming $\rho = 10^3$ kg/m^3 and $\gamma = 60$ mN/m, we find from Eq. (2) that $a_{crit,barb} = 1.9$ μm and $a_{crit,bead} = 0.1$ μm. Therefore, the predicted critical fiber diameters are $d_{crit,barb} = 3.8$ μm and $d_{crit,bead} = 0.2$ μm. Comparing these values with the measured fiber diameters in Fig. 7, we find that the measured final fiber diameters, which are close to 0.2 μm (for 2–4.5 wt%), are definitely less than the predicted critical one, $d_{crit,barb} = 3.8$ μm. Therefore, the condition for barb formation has been fulfilled. As expected, barbs were formed in the experiment in this case indeed.

Table 2
Jet morphologies at solidification versus the ratio of the characteristic charge relaxation and hydrodynamic times. At the jet origin it was $\tau_C << \tau_H$.

Ratio at solidification	$\tau_C << \tau_H$	$\tau_C < \tau_H$	$\tau_C \geq \tau_H$	$\tau_C > \tau_H$
Shape	Smooth	Beaded	Barbed	Branched
τ_C [ms]	$<<10^{-6}$	$<10^{-6}$	$\approx 10^{-4}$–10^{-6}	$>10^{-4}$

5. Summary

The detailed experimental data in the present work reveal various morphologies characteristic of PVA nanofibers electrospun from solutions with relatively low polymer concentrations (below 8 wt%). At the highest concentration of 8 wt%, the resulting nanofibers are smooth, which shows that only primary bending instability was responsible for their formation. When polymer concentration in solution decreases to 6–4 wt%, barbs develop on the jets. This phenomenon is explained theoretically as a result of relatively slow charge relaxation compared to the development of the secondary electrically driven instabilities which deform jet surface locally. When the disparity of the slow charge relaxation compared to the rate of growth of the secondary electrically driven instabilities becomes even more pronounced, the barbs transform in full scale long branches. The competition between charge relaxation and rate of growth of capillary and electrically driven secondary localized perturbations of the jet surface is affected not only by the electric conductivity of polymer solutions but also by their viscoelasticity. In addition, a nonlinear theoretical model was able to mimic the main morphological trends recorded in the experiments.

References

[1] Dersch R, Liu TQ, Schaper AK, Greiner A, Wendorff JH. Journal of Polymer Science, Part A: Polymer Chemistry 2003;41(4):545–53.
[2] Greiner A, Wendorff JH. Angewandte Chemie International Edition 2007;46(30):5670–703.
[3] Li D, Xia YN. Advanced Materials 2004;16(14):1151–70.
[4] Huang ZM, Zhang YZ, Kotaki M, Ramakrishna S. Composites Science and Technology 2003;63(15):2223–53.
[5] Reneker DH, Yarin AL, Fong H, Koombhongse S. Journal of Applied Physics 2000;87(9):4531–47.
[6] Reneker DH, Yarin AL. Polymer 2008;49(10):2387–425.
[7] Yarin AL, Koombhongse S, Reneker DH. Journal of Applied Physics 2001;89(5):3018–26.
[8] Hohman MM, Shin M, Rutledge G, Brenner MP. Physics of Fluids 2001;13(8):2201–20.
[9] Hohman MM, Shin M, Rutledge G, Brenner MP. Physics of Fluids 2001;13(8):2221–36.
[10] Koombhongse S, Liu WX, Reneker DH. Journal of Polymer Science, Part B: Polymer Physics 2001;39(21):2598–606.
[11] Yarin AL, Kataphinan W, Reneker DH. Journal of Applied Physics 2005;98(6). 064501-1-064501-12.
[12] Earnshaw S. In: On the nature of the molecular forces which regulate the constitution of the luminiferous ether, vol. 7. Cambridge: Transaction Cambridge Philosophical Society; 1842. p. 97–112.
[13] Reneker DH, Yarin AL, Zussman E, Xu H. Electrospinning of nanofibers from polymer solutions and melts. pp. 43–195. In: Advances in applied mechanics, vol 41; 2007.
[14] Yarin AL, Koombhongse S, Reneker DH. Journal of Applied Physics 2001;90(9):4836–46.
[15] Taylor G. Proceedings of the Royal Society of London, Series A Mathematical and Physical Sciences 1964;280(138):383.
[16] Larrondo L, Manley RSJ. Journal of Polymer Science Polymer Physics Edition 1981;19(6):909–20.
[17] Holzmeister A, Rudisile M, Greiner A, Wendorff JH. European Polymer Journal 2007;43(12):4859–67.
[18] Holzmeister A. Dissertation: Nanofibers as drug carriers in inhalation therapy – novel structures, methodes of preparation and surface modification. Marburg: Philipps-University Marburg; 2009.
[19] Srikar R, Yarin AL, Megaridis CM, Bazilevsky AV, Kelley E. Langmuir 2008;24(3):965–74.
[20] Srikar R, Gambaryan-Roisman T, Steffes C, Stephan P, Tropea C, Yarin AL. International Journal of Heat and Mass Transfer 2009;52(25–26):5814–26.
[21] Holzmeister A, Greiner A, Wendorff JH. Polymer Engineering and Science 2009;49(1):148–53.
[22] Han T, Yarin AL, Reneker DH. Polymer 2008;49(6):1651–8.
[23] Yarin AL. Free liquid jets and films: hydrodynamics and rheology. New York, Harlow: Longman Scientific & Technical and Wiley & Sons; 1993.
[24] Jeans JH. The mathematical theory of electricity and magnetism. Cambridge: Cambridge University Press; 1958.